Cirrus Microphysical Properties and Air Motion Statistics Using Cloud Radar Doppler Moments. Part I: Algorithm Description

MIN DENG AND GERALD G. MACE

University of Utah, Salt Lake City, Utah

(Manuscript received 29 July 2005, in final form 1 February 2006)

ABSTRACT

The first three moments of the millimeter-wavelength radar Doppler spectrum provide valuable information regarding both cloud properties and air motion. An algorithm using these Doppler radar moments is developed to retrieve cirrus microphysical properties and the mean air vertical motion and their errors. The observed Doppler spectrum results from the convolution of a quiet-air radar reflectivity spectrum with the turbulence probability density function. Instead of expressing the convolution integral in terms of the particle fall velocity as in past studies, herein the convolution integral is integrated over the air motion so that the mean vertical velocity within the sample volume can be explicitly solved. To avoid an ill-conditioned problem, the turbulence is considered as a parameter in the algorithm and predetermined from the Doppler spectrum width and radar reflectivity based on the observation that the spread of the particle size distribution in the velocity domain dominates the Doppler spectrum width measurement for most cirrus. It is also shown that the assumed single mode functional shapes cannot reliably represent significant bimodalities. Nevertheless, the IWC can be retrieved more reliably than can the mass mean particle size. Error analysis also shows that the retrieval algorithm results are very sensitive to the power-law relationships describing the ice particle mass and the terminal velocity in terms of the particle maximum length. It is estimated that the algorithm errors will be on the order of 35%, 85%, and ± 20 cm s^{-1} for mass mean particle size, IWC, and sample volume mean air motion, respectively. Algorithm validation with in situ data demonstrates that the algorithm can determine the cloud microphysical properties and air mean vertical velocity within the predicted theoretical error bounds.

1. Introduction

Cirrus clouds are recognized as an important component of the earth's climate system because of their effects on the energy and water cycles (Ramanathan et al. 1989; Randall et al. 1989; Ackerman et al. 1988; Jensen et al. 2004). With this recognition, many projects [e.g., the Atmospheric Radiation Measurement Program (ARM; Stokes and Schwartz 1994)] and field programs [e.g., The Cirrus Regional Study of Tropical Anvil and Cirrus Layer (CRYSTAL) Florida Area Cirrus Experiment (FACE); Jensen et al. 2004] have been conducted to provide better observations of cirrus properties with an ultimate goal of improving the representation of cirrus in general circulation models where their current parameterization is known to be deficient (Del Genio 1996). At the same time, many algorithms have been developed to retrieve cirrus microphysical properties by using measurements from those field programs, for example, radar–lidar (Wang and Sassen 2002), radar–radiometer (Mace et al. 1998; Matrosov 1999), lidar–radiometer (Comstock et al. 2002), and radar- (Mace et al. 2002; Matrosov et al. 2002) or lidar- (Wang et al. 2004) only algorithms. Each instrument type has its own advantages and disadvantages so that the challenge for algorithm developers is often to combine various measurements so that the natural synergy among the measurements can be exploited.

For instance, combining data from radiometer and lidar provides an opportunity to study optically thin cirrus clouds (Platt and Harshvardhan 1988; Comstock et al. 2002; Zhang and Mace 2006). The temperature inferred from the radiance measured by an infrared radiometer in the atmospheric "window" of 10–12 μm is generally lower than the blackbody brightness temperature for thin cirrus clouds. The IR emissivity of these layers is combined with a measurement of visible extinction from lidar to infer the cloud microphysical

Corresponding author address: Gerald G. Mace, Department of Meteorology, University of Utah, 135S 1460E, Rm 819 (819 WBB), Salt Lake City, UT 84112-0110.
E-mail: mace@met.utah.edu

characteristics. However, it is known that these procedures produce biased results when clouds are optically thick or have multiple layers.

Multilayered clouds occur commonly in the vicinity of deep tropical convection (Comstock et al. 2002). Over the tropical oceans, thin cirrus layers often overlie boundary layers containing significant amounts of cumulus and stratocumulus (Warren et al. 1985). Those characteristics make the algorithms using radiometer or lidar measurement inapplicable. As an alternative, the millimeter Doppler cloud radar (MMCR), because of its capabilities, is uniquely suited to study optically thick and multilayered cirrus. First, millimeter-wavelength cloud radar can often penetrate optically thick low- and midlevel clouds with minimal attenuation and provide valuable information regarding higher clouds. Second, Doppler measurements provide a backscattered power spectrum as a function of the particle fall velocity, which is related to, among other things, the particle mass (Mitchell 1996). Moreover, the second Doppler moment σ_d (see appendix B for a description of variables herein) or Doppler spectrum width, is a measurement of the spread of the signal in the Doppler velocity domain, and is attributed to the presence of particles with different terminal velocities and the turbulence within the radar sample volume. As a result, the spectrum width measurement is potentially important for the interpretation of Doppler radar data in terms of cloud dynamics.

Several algorithms have been developed to use radar reflectivity and Doppler velocity. Mace et al. (2002) and Matrosov et al. (2002) assume that at each range gate, the measured mean Doppler velocity represents the sum of the reflectivity-weighted particle fall velocities and the vertical air motion. They assume that after suitable averaging (~15–20 min), the residual air motions will be small relative to the sedimentation speeds of the particles that contribute most to the radar measurements. The radar reflectivity and corrected Doppler velocity can then be used to retrieve the microphysical properties in each radar resolution volume by assuming an exponential particle size distribution (PSD). These algorithms depend heavily on the estimation accuracy of the particle terminal velocity. The residual vertical air motion, as well as the turbulence within the radar sample volume, is a critical source of uncertainty in retrieving cloud and precipitation microphysical information. Several investigations (Gossard 1994; Babb and Verlinde 2000; Kollias et al. 2003) have suggested approaches to deconvolve the turbulence from the Doppler velocity spectrum to retrieve the properties of water clouds or drizzle. However, these approaches have not been applied to cirrus clouds.

In addition to the microphysical properties of cirrus clouds, knowledge of cirrus radiative and dynamical processes is important for understanding the maintenance of cirrus layers within the atmosphere, and this understanding is critical to develop realistic representations of cirrus in large-scale models. Few studies have evaluated the representation of cirrus in numerical models mainly because of the paucity of reliable observations that are collected on space and time scales relevant to models. Such an approach was pioneered by Heymsfield (1977), who found that cirrus properties depend strongly on the ambient vertical velocity and temperature. Heymsfield and Donner (1990) proposed a simple scheme for parameterizing ice water content (IWC) in general circulation models from the large-scale vertical velocity and temperature based on balancing the water vapor deposition and the ice particle sedimentation. This parameterization is meaningful for cirrus clouds generated in situ by synoptic-scale lifting of a moist layer (e.g., Boehm et al. 1999). However, Mace et al. (1997, 2006) show that cirrus are found in environments in which the large-scale atmosphere is weakly ascending on average, but nearly half the cirrus are observed in weak large-scale subsidence. To unveil the relationship between the cirrus properties and dynamical and radiative processes, it is important to know the vertical velocity on different scales (Gultepe and Starr 1995), but particularly on the cloud scale where saturation ratios and subsequent particle formation are determined by the magnitude of the ascent.

In this study, a new cloud property retrieval algorithm that uses the first three Doppler radar moments (radar reflectivity, mean Doppler velocity, and spectrum width) is developed to retrieve cirrus cloud microphysical properties and mean vertical air motions simultaneously, along with estimations of uncertainties. This algorithm is developed as in Gossard (1994) by first stating that the observed Doppler spectrum is the product of a convolution between a quiet-air reflectivity spectrum (i.e., a cirrus particle size distribution existing within a sample volume that has no component of air motion along the radar beam) and the air turbulence probability density function (PDF). Assuming an exponential particle size distribution and an exponential PDF of air turbulence, a set of analytical equations relating the state variables and the measured Doppler spectrum moments are developed. Once these equations are set up, we formulate the retrieval problem into a framework based on the estimation theory of Rodgers (2000). The sensitivity and error analysis are shown in section 3. In section 4, we use in situ data for algorithm validation, and a summary is given in section 5.

2. Algorithm development

In this section, the radar Doppler spectrum is first expressed in terms of the convolution between an assumed cirrus particle size distribution and a PDF of turbulence. Through integration of the Doppler spectrum, the first three radar Doppler moments are then related to a state vector (particle size distribution and air turbulence parameters). These equations compose our forward model. Following a forward-model sensitivity study, a method to make an initial guess is proposed and the inversion formalism is discussed.

a. The quiet-air Doppler spectrum

First, by considering the quiet-air radar volume, the water-equivalent radar reflectivity factor Z_e is expressed as

$$Z_e = \int_0^\infty a_z D^{6+b_z} N(D)\, dD = \int_0^\infty S(D)\, dD, \qquad (1)$$

where the parameters a_z and b_z are constants found through a power-law function describing the radar backscatter cross section (Aydin and Walsh 1999; Mace et al. 2002), in terms of the particle maximum dimension (D). Here, $N(D)$ represents the particle size distribution. Rayleigh scattering is assumed in Eq. (1), which is valid for particles less than 800 μm at 35-GHz wavelength (Donovan et al. 2004). So the radar reflectivity density function is defined as

$$S_z(D) = a_z D^{6+b_z} N(D). \qquad (2)$$

Some researchers have suggested that the particle size versus number concentration spectra can be well represented by one or more exponential regimes (Mace et al. 2002). Here we consider a simple exponential function to describe the PSD, and then the quiet-air spectrum density function becomes

$$S_z(D) = a_z N_o \exp(-\lambda D) D^{6+b_z}, \qquad (3)$$

where N_o is the particle concentration intercept and λ is the exponential slope. However, the observed radar Doppler spectrum is a function of Doppler velocity. Fortunately, the relationship between the ice particle terminal velocity in quiet air and the ice particle size has been studied and can be fitted by a power-law function according to in situ measurements (e.g., Heymsfield and Iaquinta 2000; Mitchell 1996),

$$D\ (\text{cm}) = a_d V_f^{b_d}, \qquad (4)$$

where a_d and b_d are parameters of the power-law fit function. This equation is equivalent to $V_f = a_v D^{b_v}$, where the a_v and b_v coefficients are A and B in the fall-speed power law in Mace et al. (2002). Because the relationship between size and fall velocity is usually given as the later form in published literature, there will be an additional uncertainty in the coefficients a_d and b_d.

With Eq. (4), the transformed quiet-air reflectivity spectral density function in terms of the particle fall velocity is

$$S(V_f) = N_o a_z b_d a_d^{(7+b_z)} V_f^{[b_d(7+b_z)-1]} \exp(-\lambda a_d V_f^{b_d}). \qquad (5)$$

b. The convolution of the quiet-air Doppler spectrum with turbulence

The actual reflectivity spectrum $S(w_i)$ is derived through a convolution of the quiet-air spectrum $S(V_f)$ with a PDF function $G(w_j)$ of turbulence (Gossard 1994; Babb and Verlinde 2000):

$$S(w_i) = \int_{-\infty}^{w_i} G(w_j) S[V_f = (w_i - w_j)]\, dw_j, \qquad (6)$$

where w_i and w_j are Doppler velocity and air vertical velocity, respectively. The limit of the integration is $(-\infty, w_i)$, because there are no quiet-air ice particles with upward velocity. In other words, the air velocity is always smaller than the Doppler velocity because we assume that downward motion is positive. In comparing with Gossard (1994), Eq. (6) is parallel to his Eq. (12a), which is limited between $(0, \infty)$ for the particle fall velocity integration. However, here we have invoked the commutative principle so that we can express the air turbulence PDF explicitly in terms of the mean vertical air motion and we integrate the convolution integral with respect to the air velocity rather than the particle fall velocity.

Following Gossard (1994), the distribution of air turbulence can be approximated by an exponential PDF given by

$$G(w_j) = \frac{1}{2W_\sigma} \exp\left(-\frac{|w_j - W_m|}{W_\sigma} \right), \qquad (7)$$

where W_m is the mean air vertical velocity, $1.4W_\sigma$ is the standard deviation of the vertical motion and represents the turbulent intensity (hereinafter called the std dev of the vertical motion). In Fig. 1, the solid line with an asterisk is an example of the turbulence PDF obtained from 15 s of 25-Hz vertical velocity data measured by the University of North Dakota (UND) Cita-

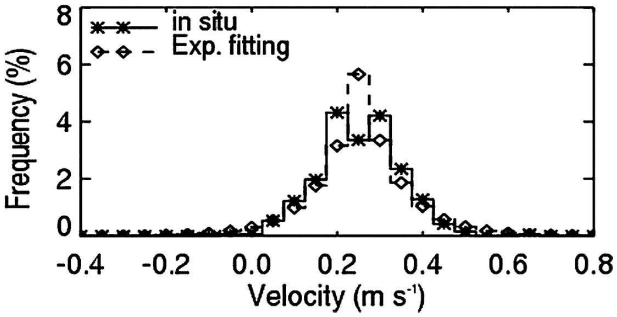

FIG. 1. The PDF of turbulence in 15 s of 25-Hz air velocity data measured by the UND Citation aircraft. The solid line with an asterisk represents the in situ measurements. The dash line with a diamond represents an exponential fit with Eq. (7) in the text.

tion aircraft during the spring 2000 intensive observation period (IOP) at the ARM Southern Great Plains (SGP) site. Gossard (1994) has demonstrated that this convolution technique is not very sensitive to the exact functional form chosen for the turbulence PDF.

With the convolution model, the observed reflectivity spectral density at the ith Doppler velocity bin is a function of N_o, λ, W_m, and W_σ. Substituting Eqs. (5) and (7) into Eq. (6), we have the turbulence-convolved spectral density function in Eqs. (8) and (9) in two different Doppler velocity ranges:

$$S_{z1}(w_i) = \frac{1}{2w_\sigma}\int_{-\infty}^{w_i} S_0(w_i - w_j)^{b_d(7+b_z)-1} \times \exp[-a_d\lambda(w_i - w_j)^{b_d}]\exp\left(\frac{w_j - w_m}{w_\sigma}\right) dw_j \tag{8}$$

for $(w_i < w_m)$ and

$$S_{z2}(w_i) = \frac{1}{2w_\sigma}\left\{\int_{-\infty}^{w_m} S_0(w_i - w_j)^{b_d(7+b_z)-1}\exp[-a_d\lambda(w_i - w_j)^{b_d}]\exp\left(\frac{w_j - w_m}{w_\sigma}\right) dw_j + \int_{w_m}^{w_i} S_0(w_i - w_j)^{b_d(7+b_z)-1}\exp[-a_d\lambda(w_i - w_j)^{b_d}]\exp\left(\frac{w_m - w_i}{w_\sigma}\right) dw_j\right\} \tag{9}$$

for $(w_i > w_m)$. The net effect of convolution is to broaden and shift the original quiet-air signal. Figure 2 shows the broadening (resulting from the turbulence) and shifting effects (resulting from the air mean velocity) of air motions to the quiet-air Doppler spectrum (solid line). As the air mean upward motion increases, the convolved Doppler spectrum shifts to negative Doppler velocity. As w_σ increases, the Doppler spectrum broadens.

Through Eqs. (8) and (9), we can calculate the moments of the radar Doppler spectrum by integration. The radar reflectivity Z_e, mean Doppler velocity V_d, and Doppler spectrum width σ_d can be expressed as

$$Z_e = \int_0^\infty S_z(D)\, dD = \int_{-\infty}^\infty S(w_i)\, dw_i, \tag{10}$$

$$V_d = \frac{\int_{-\infty}^\infty S(w_i) w_i\, dw_i}{\int_{-\infty}^\infty S(w_i)\, dw_i}, \quad \text{and} \tag{11}$$

$$\sigma_d^2 = \frac{\int_{-\infty}^\infty S(w_i)(w_i^2 - V_d^2)\, dw_i}{\int_{-\infty}^\infty S(w_i)\, dw_i}. \tag{12}$$

The ensemble cirrus properties such as IWC, mass-weighted mean particle size D_{mass}, and mass-weighted particle fall velocity $V_{f\text{mass}}$ can be derived from the retrieved particle size distribution.

IWC can be derived by integrating the individual particle mass over the particle size distribution. For the exponential PSD considered here, by using a mass-sized power-law relationship

$$M(D) = a_m D^{b_m}, \tag{13}$$

where a_m and b_m are the power-law parameters, the IWC can be estimated as

$$\text{IWC} = \int_0^\infty a_m D^{b_m} n(D)\, dD = a_m b_m \Gamma(b_m) N_o \lambda^{-(b_m+1)}. \tag{14}$$

The $V_{f\text{mass}}$ can be derived analytically as

$$V_{f\text{mass}} = \frac{1}{\text{IWC}}\int_0^\infty m(D) V_f(D) n(D)\, dD = a_v(1 + b_v/b_m)\Gamma(b_m + b_v)/\Gamma(b_m)\lambda^{-b_v}. \tag{15}$$

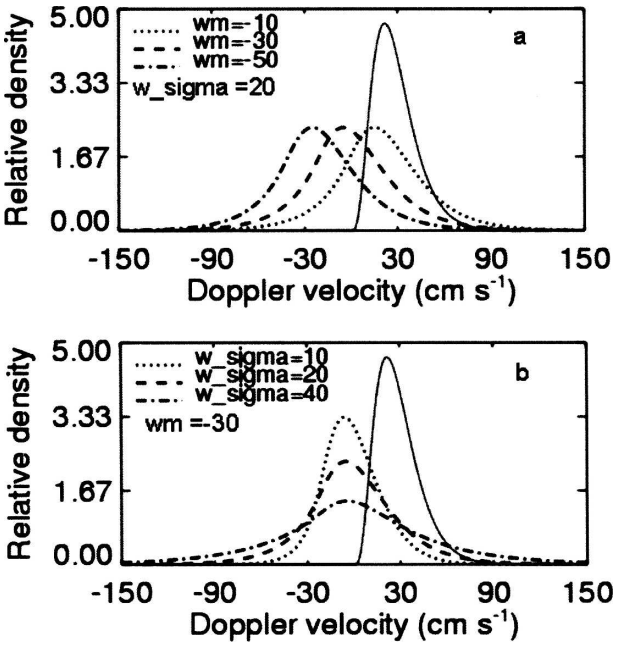

FIG. 2. Simulated relative reflectivity density spectra with different inputs of (a) W_m and (b) W_σ. The solid black line is the quiet-air Doppler spectrum. In this simulation, $N_o = 1.0 \times 10^5$ and $\lambda = 250$ (cgs). The parameters used in this simulation are 1.2×10^{-4}, 1.92, 1000.00, and 1.1 for a_m, b_m, a_v, and b_v, respectively.

In the same way, the D_{mass} can be written as

$$D_{\text{mass}} = \frac{b_m + 1}{\lambda}. \tag{16}$$

Actually, the power laws, as published, represent limited particle size ranges and are not strictly applicable for integration over a full particle size distribution as we apply them here. Using a single power law for integration convenience adds to the uncertainty of the retrieval algorithm and will be an issue that will addressed in future implementations of this algorithm. It should be noted, however, that the use of single power laws to represent full PSDs is a common practice in most cirrus retrieval algorithms, with the exception of the innovative work described in Matrosov et al. (2002).

c. *The optimal estimation framework and the initial guess of the solution*

In the last section, we showed how the first three Doppler moments could be described analytically as functions of N_o, λ, W_m, and W_σ by assuming that the radar backscattering cross section and terminal velocity follow power-law relationships with respect to the PSD. Based on Eqs. (10)–(12), a forward model of the Doppler radar observations can be formulated that relies on the PSD and turbulence PDF. In this forward model, we also assume values of the model parameters (a_z, a_d, b_z, and b_d) according to in situ data studies (Mitchell

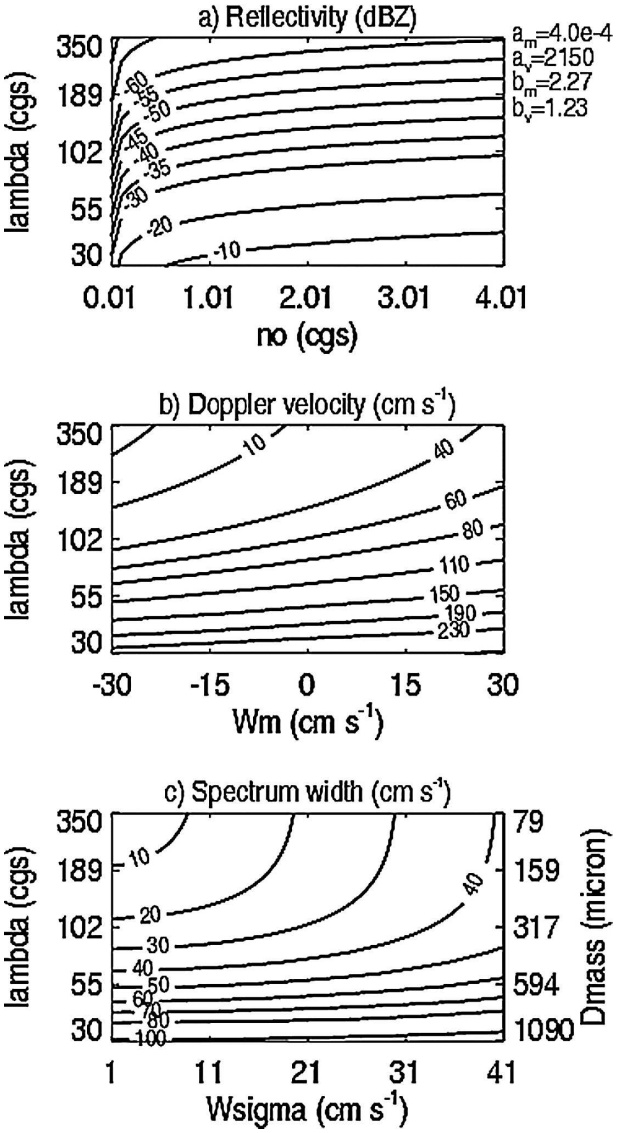

FIG. 3. Forward model sensitivity to inputs N_o, λ, W_m, and W_σ. (a) The sensitivity of radar reflectivity to λ and N_o, (b) the sensitivity of Doppler velocity to λ and W_m, and (c) the sensitivity of spectrum width to λ and W_σ. The y axis is also labeled as D_{mass} on the right side. The parameters used in this study are the same in Fig. 2.

1996; Heymsfield and Iaquinta 2000). The response of the forward model is shown in Fig. 3 and can be summarized in the following three relationships:

$$Z_e = f(\lambda, N_o), \tag{17}$$

$$V_d = f(\lambda, W_m), \quad \text{and} \tag{18}$$

$$\sigma_d = f(\lambda, w_\sigma). \tag{19}$$

The sensitivity study shows that each of the radar moments is primarily dependent on two of the forward-

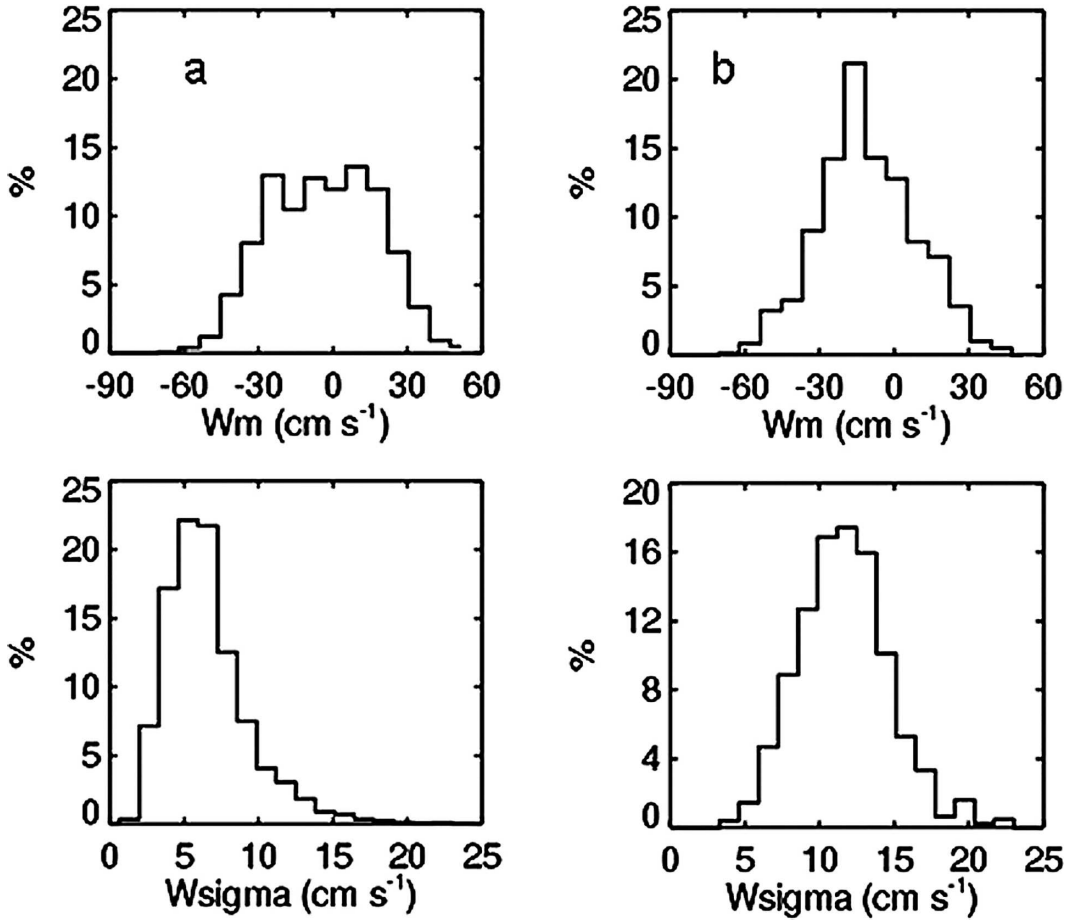

FIG. 4. The frequency distribution of W_m and W_σ obtained from in situ measurements. (a) From 15-s averages of 25-Hz UND Citation observations on 9 and 13 Mar 2000 at the ARM SGP. (b) From 1 min of 1-Hz WB57 data collected on 29 Jun, and 13 and 31 Jul during the CRYSTAL FACE project. There are 14 484 and 10 145 sets of W_m and W_σ for SGP and CRYSTAL FACE, respectively.

model input variables, and all depend on λ. The radar reflectivity is determined only by the particle size distribution, the mean Doppler velocity is the quiet-air Doppler fall velocity of the particle size distribution shifted by the mean air motion, and the Doppler spectrum width is determined by the variance of the particle size distribution and the turbulence intensity. The inversion problem, as we have posed it here, is ill conditioned, with three measurements to solve for four unknowns. To address this problem, we could resort, for instance, to Z_e–IWC empirical relationships (e.g., Liu and Illingworth 2000) as a fourth source of information. However, such empirical relationships have significant uncertainties as shown in observations and theory (Atlas et al. 1995). Therefore, in the current algorithm, W_σ is not retrieved but is considered as a parameter and estimated as described below.

Our rationale to estimate W_σ is based on two facts. First, the observed range of W_σ around cirrus clouds is typically small. Figure 4 shows the PDF of W_σ and W_m calculated from aircraft in situ data collected at the ARM SGP site during the 2000 cloud IOP and in the Tropics during CRYSTAL FACE. Figure 4a is derived from 15 s of 25-Hz vertical velocity data collected by the UND Citation on 9 and 13 March at the ARM SGP site, and in Fig. 4b W_m and W_σ are obtained from 1 min of 1-Hz vertical velocity data measured by the WB-57F aircraft on 29 June, and 13 and 31 July 2002 during the CRYSTAL FACE campaign. Using approximately 5 h of in situ data from the midlatitudes and Tropics, we find that W_σ tends to be distributed between about 5 and 15 cm s^{-1}. Second, from the forward-model response (Fig. 3c) we know that of the Doppler radar measured quantities, only the Doppler spectrum width depends on W_σ. In Fig. 3c, the simulated Doppler spectrum width is also labeled as a function of D_{mass} on the right-hand axis. We find that, in the range of D_{mass} for cirrus (100–850 μm) and with W_σ as found in aircraft

data, the spectrum width is nearly insensitive to W_σ in the range in which W_σ is observed in most cirrus.

To estimate W_σ we rely on the fact that the Doppler spectrum width in cirrus (σ_d) is attributed primarily to the slope of the particle size distribution (λ) and the breadth of the turbulence PDF (W_σ). Furthermore, physically W_σ is always less than σ_d, and, for the same Doppler spectrum width, the larger λ is, the larger W_σ is. At the same time, the radar reflectivity is inversely related to a certain power of λ [by the integration of Eq. (10)]. Slope λ indirectly indicates the dispersion of the particle fall velocity because the larger the λ is, the more likely there is to be a broad PSD and thus a broad particle fall velocity distribution. Thus, the breadth of the turbulence PDF (W_σ) is estimated empirically as a function of the magnitude of the Doppler spectrum width (cm s^{-1}) and the radar reflectivity (dBZ):

$$W_\sigma = a_w \sigma_d^{b_w} \frac{|Z_e|}{\max(|Z_e|)}, \tag{20}$$

where a_w and b_w are empirically derived constants. The maximum of absolute Z_e is about 40 because the minimum detectable radar reflectivity of MMCR at cirrus altitudes is -40 dBZ. Equation (20) is only appropriate for cirrus with Z_e less than 0 dBZ, which is the case for most cirrus clouds. When the reflectivity is small (i.e., the absolute value of Z_e in dBZ is larger) the turbulence has a larger contribution to spectrum width. Here, a_w and b_w are derived using in situ vertical velocity data and MMCR observations collected in cirrus during 9 and 13 March 2000 at ARM SGP. The results are shown in Fig. 5. The fitted parameters are 4.95 and 0.45 for a_w and b_w, respectively. The correlation coefficient between the fitting (solid line) and the observation (black cross) is about 0.8. For cirrus with Z_e greater than 0 dBZ, W_σ is set as the mean value (10 cm s^{-1}) of the in situ observation discussed in the previous paragraph. From the forward-model sensitivity study, we can see that Doppler spectrum width is primarily determined by the dispersion of the particle fall velocities when the radar reflectivity is larger than 0 dBZ. The uncertainty of the final solution resulting from the W_σ estimation error will be investigated in the next section.

A flowchart for estimating the first guess of the algorithm solution is shown in Fig. 6. Once W_σ is estimated through σ_d and Z_e, λ is approximately determined through the observed Doppler spectrum width and W_σ. After that, N_o is approximated from Z_e and λ. The air mean velocity is approximated from V_d and the relationship of terminal velocity versus length. The first guess provides a reasonable approximation of the solution that is then used in the inversion algorithm. The

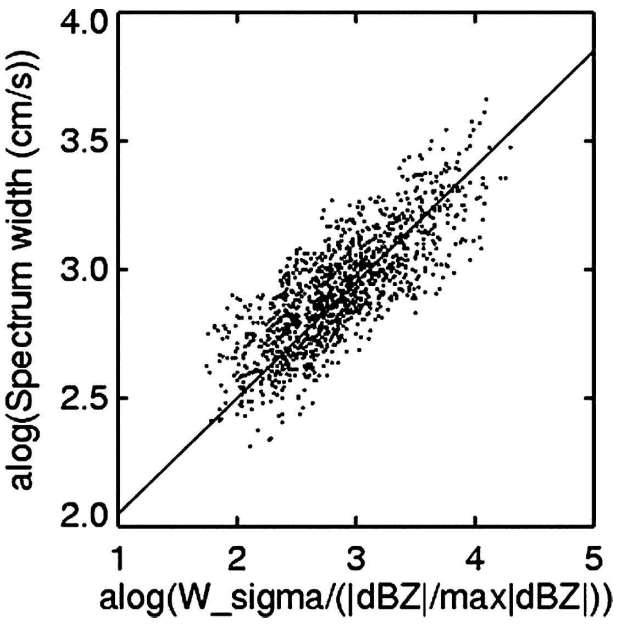

FIG. 5. Derivation of an empirical formula relating W_σ to Doppler spectrum width and reflectivity (Z_e, dBZ). The scatterplot of the Doppler spectrum width to the ratio of W_σ to reflectivity (dBZ) is fitted with Eq. (20) in a solid line.

inversion technique is based on optimal estimation theory (Rodgers 2000). This technique uses a Gauss–Newton iterative scheme to minimize the gradient of a cost function that balances uncertainties in the first guess, the observations, and the model parameters to determine N_o, λ, and W_m along with their uncertainties from the first three Doppler radar moments. Because the inversion algorithm assumes that the problem is reasonably linear, we use perturbations up to 80% to each variable in the initial guess to test whether the solution can converge. The results (figures not shown) show that the solution of PSD parameters can converge to within 30% uncertainty for up to 80% perturbation in their initial guess. However, the mean vertical air motion retrieval is very sensitive to its initial guess. It will bypass 30% uncertainty when its initial guess is underestimated by 50%. However, from the flowchart we can see that the initial guess first gets the PSD parameter, then W_m. This flowchart can partially decrease the deviation of the initially guessed W_m from actual solution, and hence improve the nonlinear problem.

As derived above, the forward model requires specification of six empirical parameters for the fall velocity, radar backscatter cross section, and mass as a function of maximum particle dimension using power-law relationships. However, the backscatter cross section for small spherical crystals is a function of the sixth moment of the particle volume–equivalent length (Ma-

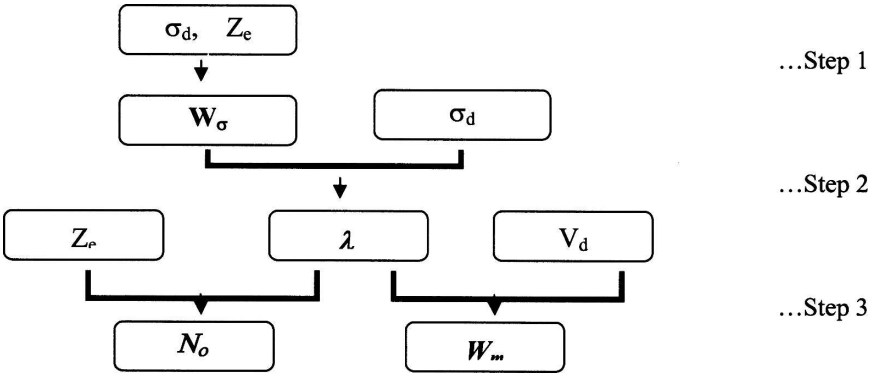

FIG. 6. The schematic flowchart for determining a first approximation in the variational inversion algorithm.

trosov 1993; Donovan et al. 2004), which is positively related to the particle maximum length through the mass–length relationship [see Eq. (A7) in appendix A]. As a result, the parameters in the backscatter cross-sectional power-law relationship are strongly correlated to those parameters in the mass power-law relationship. In appendix A, this dependence is deduced through both the effective ice particle density–length relationship and the mass–length relationship using a spherical model for cirrus particles. As a result, only four parameters rather than six are actually unique (see appendix A): a_m, b_m, a_d, and b_d. Although a_d and b_d are related to a_m and b_m through a particle cross-sectional area power-law relationship (Mitchell 1996), the derivation is tedious and does not reduce the number of parameters. Using Eq. (A2), we can derive a_z and b_z from a_m and b_m. These parameters are typically deduced from in situ data and depend on the particle size and crystal habit (Heymsfield 2003, Heymsfield et al. 2004). The uncertainties resulting from the possibility of biased power-law fit parameters will be investigated in the following section. In this paper, the parameters for algorithm retrieval are adapted from published works (Heymsfield and Iaquinta 2000; Mitchell 1996) and assumed to vary as a function of temperature and pressure.

3. Algorithm error analysis

The accuracy of the retrieval results depend on the degree of accuracy of the assumptions in the forward model and uncertainties in the forward-model power-law fit parameters, while the precision of the results depends also on observational uncertainties. In the following paragraphs, we focus on the sensitivity of the retrieval results to the exponential particle size distribution assumption and the model parameters (a_m, b_m, a_d, b_d, and W_σ). This error analysis sheds some light on the veracity of the algorithm results and presents paths toward improving the retrieval algorithm as additional empirical information becomes available.

a. Sensitivity to the exponential PSD assumption

The PSD can be modeled using different mathematical functions. A detailed analysis of aircraft-observed particle-sized spectra is shown in Mace et al. (2002) and Heymsfield et al. (2004). It is well known that aircraft-observed PSDs can be fitted with single-mode exponential or Gamma functions or with combinations of these functions to create a bimodal distribution. For instance, an exponential distribution for the small particles and a gamma distribution for the large particles were used in Mace et al. (2002). The modified gamma function is described as

$$N(D) = N_g e^{\alpha}(D/D_g)^{\alpha} \exp[-\alpha(D/D_g)],$$

where N_g is a proportionality constant, D_g is the size where the function $N(D)$ maximizes, and α indicates the breadth of the spectrum, where α can vary from 1 to 20. The larger it is, the narrower the spectrum is. With three adjustable parameters, the modified gamma function can fit unimodal PSDs to a high level of precision. The modified gamma distribution is also used as a two-parameter function by assuming a fixed α (Gossard 1994; Mace et al. 1998, 2005). Even though both the exponential and the fixed α-modified gamma functions use two parameters, the exponential PSD always includes small particles while the gamma distribution can be biased to the large particles. Figure 7 shows the exponential PSD and gamma distributions for α equal to 1, 3, and 5 for an IWC of 13 mg m^{-3} and radar reflectivity of -24.0 dBZ. We can see that, relative to the exponential distribution, the gamma distribution tends to have fewer particles in the distribution ex-

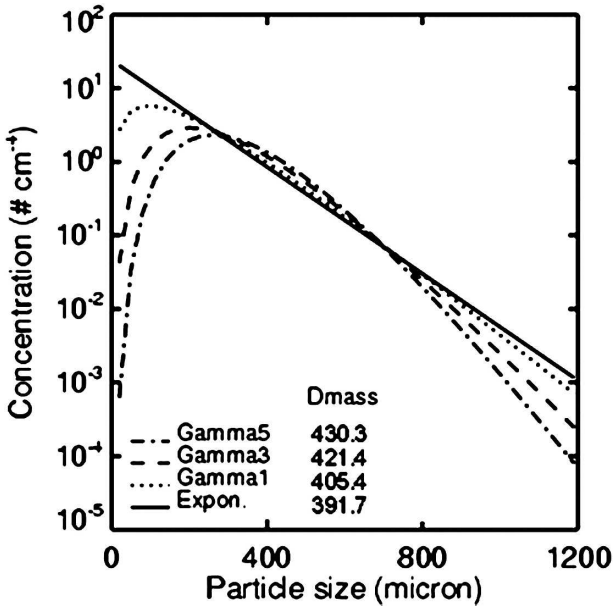

FIG. 7. The exponential PSD and gamma PSD with α equal to 1, 3, and 5 for which the IWC and radar reflectivity are the same. The corresponding mass mean length (D_{mass}) is noted in the lower-left corner.

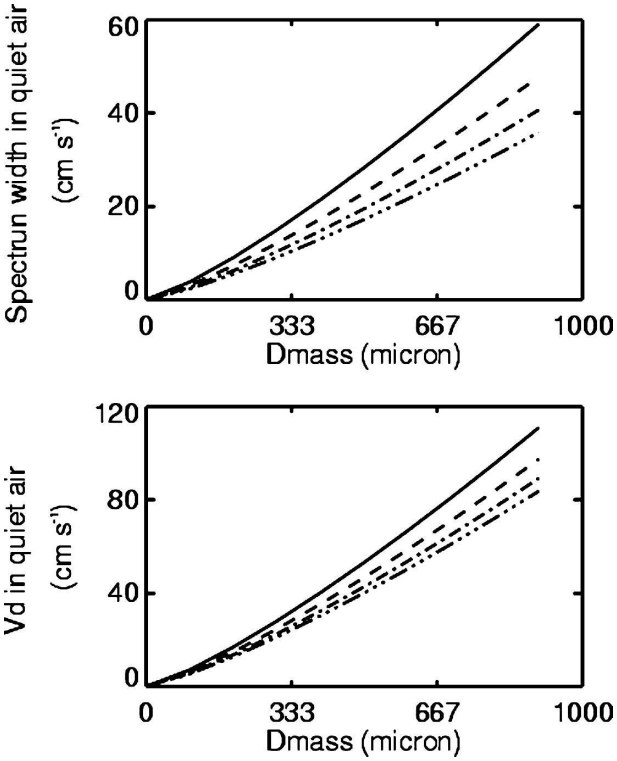

FIG. 8. The quiet-air Doppler velocity and spectrum width as a function of D_{mass} for the exponential PSD (solid line) and gamma PSD with α equal to 1, 3, and 5 (dash, dot–dash, and triple dot–dash line, respectively). For the same D_{mass}, the exponential PSD has the largest Doppler velocity and spectrum width in the quiet air.

tremes, especially for small particles. This results in the largest mass mean length (denoted in the lower-left corner) for the gamma function with α equal to 5.

The algorithm we describe in this paper only uses radar observations without other measurements such as the lidar extinction or emittance from an IR radiometer. The difference between the exponential and fixed gamma distributions might be important for the retrieval of particle size. For example, the quiet-air Doppler velocity and spectrum width as a function of D_{mass} are plotted in Fig. 8 for exponential (solid line) and gamma distributions assuming α is equal to 1, 3, and 5 (dash, dot–dash, and triple dot–dash, respectively). We can see that, for the same D_{mass}, the exponential PSD has the largest Doppler velocity and spectrum width. In other words, for a given Doppler velocity and spectrum width an exponential PSD would result in the smallest particle size. As a result, the accuracy of the retrieved particle size depends on how closely the assumed PSD in the algorithm represents the actual PSD. In the following, we explore the effect of the assumed particle size distribution on this algorithm using in situ data measured by the UND Citation aircraft during the March 2000 IOP at the ARM SGP site. The parameters (W_m and W_σ) are calculated with Eq. (7) from 15-s intervals of 25-Hz Citation data as in Fig. 4. The PSDs are reconstructed from both UND two-dimensional cloud probe (2DC) and forward-scattering spectrometer probe (FSSP) data ranging from 30 to 1000 μm. The particle sizes are calculated from raw 2DC image data using the particle reconstruction method in Heymsfield and Parrish (1978), which allows the size of particles that are off the edge of the diode array to be estimated. The FSSP 1-Hz data, provided by M. Poellot of UND, were used for particle distributions below 50 μm. The procedure for this sensitivity study is to compute the radar moments from the aircraft vertical velocity and particle spectra using numerical integration. Then, the microphysical properties and air mean velocity are retrieved with the algorithms assuming an exponential PSD or modified Gamma PSD with α equal to 3 or 5.

Several examples of in situ particle size spectra and corresponding retrievals are shown in Fig. 9. In each panel, the triangle, asterisk, and diamond represent in situ observations, exponential PSD retrieval, and gamma PSD retrieval with α equal to 5, respectively. The results illustrated in Fig. 9a favor the exponential PSD assumption even though the in situ PSD has somewhat smaller concentrations of large particles leading to an estimate of D_{mass} from the exponential assumption that is slightly larger than the in situ measurements. In

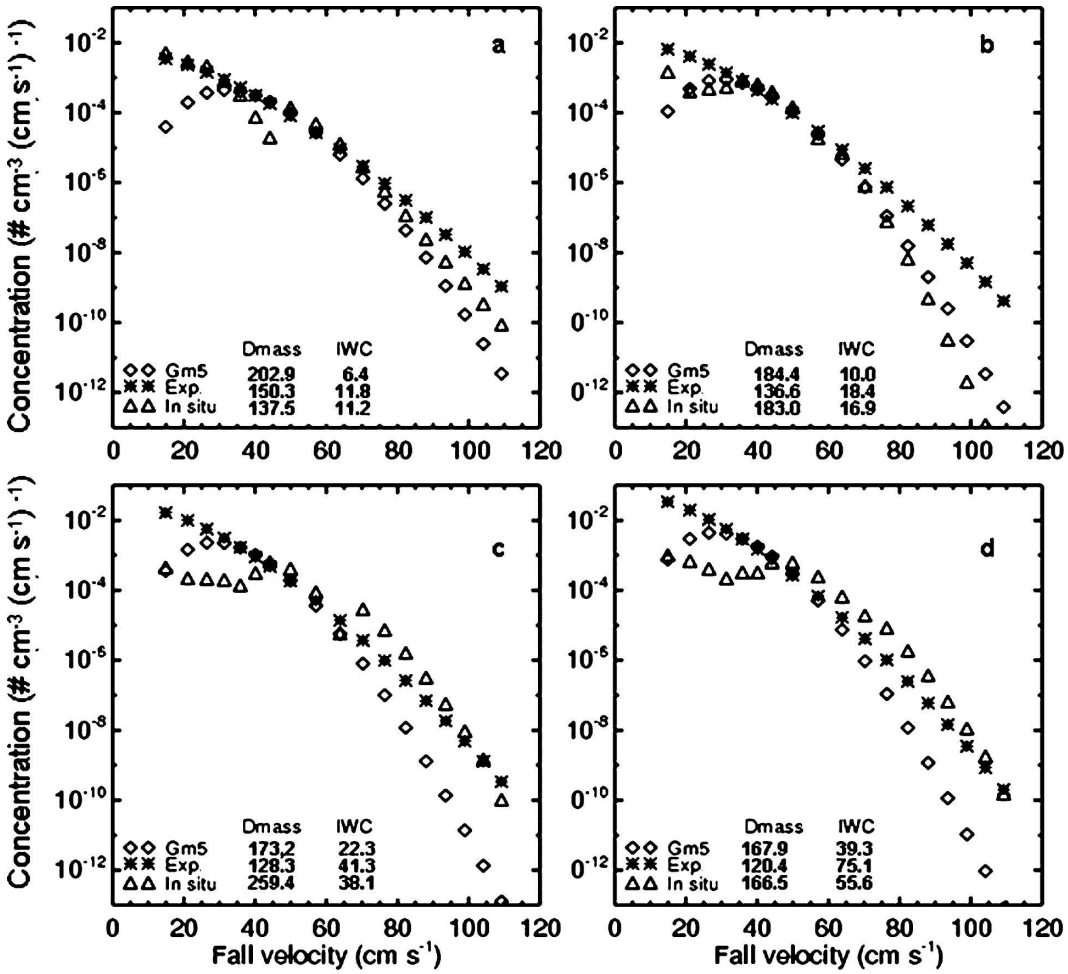

FIG. 9. Examples of in situ observed PSD in comparison with the exponential PSD and gamma PSD with α equal to 5 derived from the retrieved PSD parameters. The in situ PSD, the retrieved exponential PSD, and the retrieved gamma PSD with α equal to 5 are represented by the triangle, the asterisk, and the diamond. (a) The exponential PSD retrieval best represents the in situ PSD, (b) the gamma PSD retrieval represents the observations better than the exponential function, and (c) the in situ PSD is slightly bimodal. The exponential PSD and gamma PSD retrievals underestimate the particle size by about 40% and 25%. (d) The observed PSD is significantly bimodal. The exponential PSD and gamma PSD retrievals underestimate the particle size by about 60% and 30%. The units of D_{mass} and IWC are micrometers and milligrams per meter cubed, respectively.

Fig. 9b, the concentration of small particles is smaller and the gamma PSD retrieval does better. The case in Fig. 9c begins to show bimodality. Even though the assumed exponential PSD or gamma PSD could have the same integrated radar moments, the retrieval underestimates the ensemble mass-weighted particle length by about 40% and 25%, respectively, because the single-mode distribution functions overestimate the concentration of small particles. In Fig. 9d, bimodality is even more significant so that the exponential PSD and gamma PSD retrieval underestimate the particle size by about 60% and 30%, respectively.

For comparison, the dataset is grouped into seven classes based on the correlation coefficient r between the second moment of the retrieved exponential PSD and that of the in situ PSD. The ranges of r for the seven comparison classes are listed in Table 1.

The comparison results are shown in Fig. 10. The cases shown in Fig. 9 are included in class 1, 3, 4, and 7, respectively. We find that the exponential PSD generally results in the smallest size and largest air velocity (positive is downward motion), even for the smallest upward motion. In comparing the retrieval with the in situ measurements, the exponential PSD retrieval works well for the first two classes, where the in situ PSD is reasonably approximated by an exponential PSD. However, as the concentration of small particles decreases, the gamma PSD retrieval with α equal to 5

TABLE 1. The range of r (the correlation coefficient between the second PSD moments from in situ data and the retrieved exponential PSD second moment) for the seven classes of the PSD sensitivity study; refer to Fig. 10.

No. of classes	r
1	0.8–1.0
2	0.6–0.8
3	0.4–0.6
4	0.2–0.4
5	0.0–0.2
6	−0.3–0.0
7	−1.0 to −0.3

agrees better with the measurements. As we can see, the two-parameter PSD functions are applicable for retrieving particle size only where the actual PSD is not significantly bimodal, such as for the cases in classes 5–7. Nevertheless, the IWC can be retrieved with better precision generally than the particle size. Accurate retrieval of bimodal PSDs will require additional independent information such as lidar-derived visible extinction or perhaps full Doppler spectra instead of just the moments of the Doppler spectrum.

To develop a means for estimating when a particle distribution assumption is most appropriate for the PSD, we plotted the corresponding mean and standard deviation of temperature, the normalized distance to the cloud top, and three radar moments in Fig. 11. The number of cases in each class is noted in the radar reflectivity panel. There are totally about 1800 cases, while about 85% are in the first four classes. These results are consistent with the results in Mace et al. (2002) in which they show that although particle spectra with bimodal tendencies are common, single-mode functions are able to capture the essential characteristics of these spectra within observational uncertainty for most cirrus. This figure is also consistent with Fig. 2 in Mace et al. (2002), which shows that the possibility of significant bimodality increases for warmer temperatures and larger radar reflectivity.

The deviations of the retrieval from in situ measurements as well as the mean and standard deviation (under the dash) of the five indicators plotted in Fig. 11 are listed in Table 2 for both the exponential PSD and gamma PSD retrievals. As r between the actual PSD and the retrieved exponential PSD decreases, the mean of the temperature, the normalized distance to cloud top, and the radar reflectivity changes almost monotonically. We find that for the first four classes, the retrieval using the exponential PSD function reproduces the mass mean particle size and IWC to within 40% and 10% uncertainty and within 10 cm s^{-1} deviation for W_m. For the next three classes, the gamma PSD

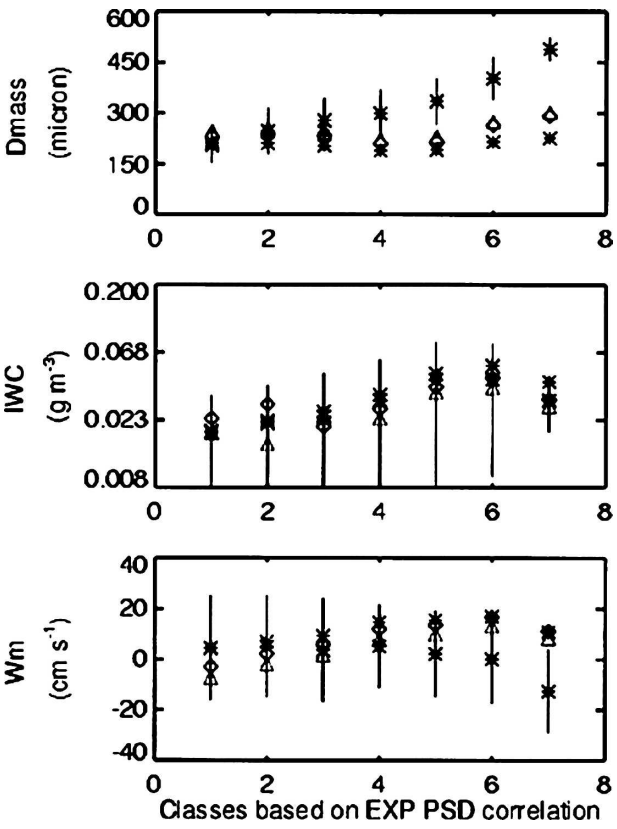

FIG. 10. The comparison of the exponential PSD retrieval (dark asterisks) and the gamma PSD retrievals (diamonds, $\alpha = 3$; triangles, $\alpha = 5$) with in situ measurements (dark asterisks with error bars) in the seven correlation classes, which are defined by the correlation coefficient (r) between the second PSD moments from in situ data and the retrieved exponential PSD second moment.

with $\alpha = 5$ produces more accurate retrievals, especially for IWC. Therefore, as a criterion (underlined in Table 2), when the normalized distance to the cloud top is larger than 0.4, the cloud temperature is warmer than 235 K, and the reflectivity is larger than −20 dBZ, a modified gamma function with $\alpha = 5$ is more appropriate for the PSD. For the full in situ dataset examined here, the average of the retrieved error resulting from the PSD assumption for the IWC, D_{mass}, and W_m are within 25%, 20%, and ±10 cm s^{-1}, respectively. Because none of the other uncertainties mentioned earlier are considered in this observation simulation study, these error estimates should be regarded as absolute lower limits on the algorithm uncertainty that will likely not be obtained in actual practice.

b. The sensitivity to the estimation of W_σ

The algorithm uncertainties resulting from the estimation of W_σ are examined by simulating the radar Doppler moments using the fitted exponential PSD and

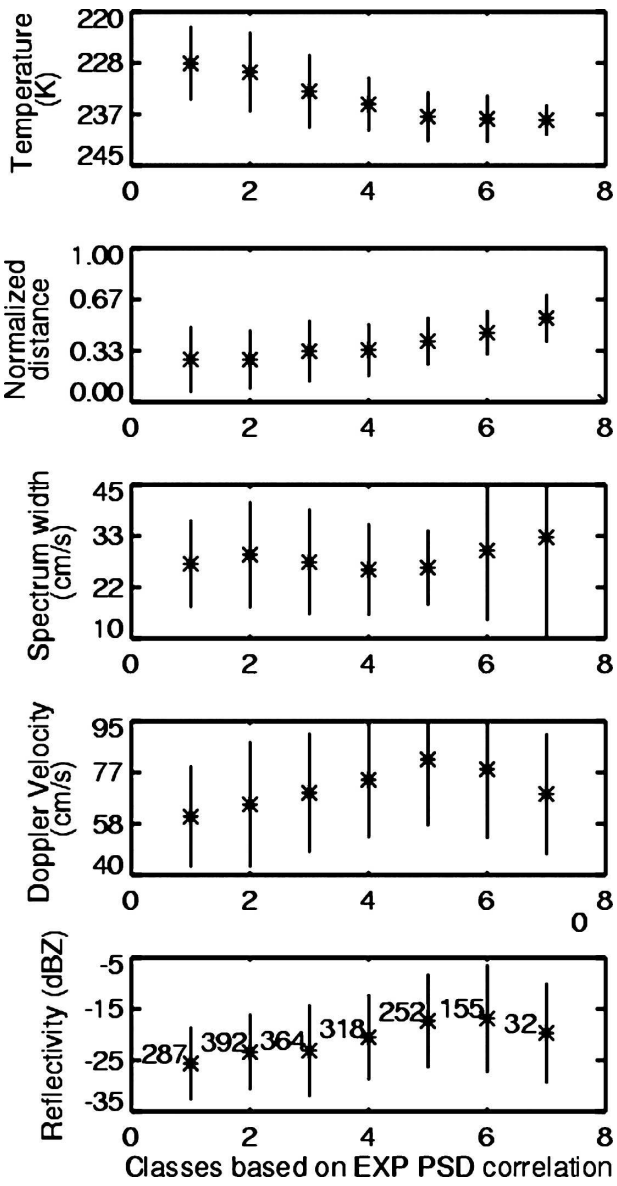

FIG. 11. The mean and standard deviation of the temperature, the normalized distance to the cloud top, and the three radar Doppler moments of the seven classes (cf. Fig. 10 and the text). The number of the cases in each class is noted in the radar reflectivity panel. In total, there are about 1800 cases. About 85% of the cases are in the first four classes, which has a PSD that can be represented reasonably with an exponential or gamma PSD.

fitted exponential PDF of turbulence from the in situ data during the March 2000 IOP at the ARM SGP. From these simulated radar moments, the retrieval is calculated by reasonably deviating the estimation of W_σ by ±40% or ±20% from the actual value, and then comparing the retrieval with the results from the unperturbed W_σ. The results are shown in Fig. 12. When W_σ is overestimated, the retrieved λ is larger than the true value, the retrieved D_{mass} and W_m are underestimated, and the IWC is overestimated. The reverse is true if W_σ is underestimated. However, the uncertainties of D_{mass} and IWC are different for different particle sizes. For the larger particle size and smaller IWC, the uncertainty is very small; for the smaller particles, the error caused by a 40% deviation of W_σ could be as large as 50% for the mass mean length and 30% for the IWC. This is consistent with the results shown in Fig. 3c. For the smaller particles, the contribution of W_σ to the Doppler spectrum width becomes significant, whereas the retrieval would be more sensitive to the estimation of W_σ. This sensitivity study illustrates that this algorithm may have relatively large uncertainties when the particle sizes are small and the effect of turbulence on the spectrum width is large. The mean and standard deviation of the retrieval from different W_σ estimations are shown in Table 3.

c. *The sensitivity to the power-law fit parameters*

Retrieval errors also arise from other sources of uncertainty such as the power-law parameters in the empirical relationships (a_m, b_m, a_d, and b_d). The sensitivity of the algorithm results to these parameters is examined in a similar way using 1500 sets of radar moments simulated from the forward model based on aircraft data observed on 9 and 13 March 2000 at the ARM SGP site. With the forward inputs, we get the true value of D_{mass}, IWC, and W_m. Their mean and standard deviation are 218 ± 50.4 μm, 8.66 ± 15.3 mg m^{-3}, and −32.3 ± 41.0 cm s^{-1} for D_{mass}, IWC, and W_m, respectively. By changing one empirical parameter at a time by ±20% and keeping the others constant, the retrieval is compared with the unperturbed result. The uncertainty of D_{mass} and IWC is shown in terms of the relative deviation (%). For W_m, the uncertainty is shown in absolute deviation in centimeters per second. The three numbers in each cell in Table 4 are the mean, maximum, and minimum of the deviation from the truth. IWC is sensitive to all parameters, while D_{mass} and W_m are not sensitive to a_m. In comparing the results, the retrieved D_{mass} is very sensitive to b_m, which is comparable in magnitude to the error that arises from the uncertainty in the estimated W_σ. The retrieved IWC is also very sensitive to b_m. The vertical velocity is very sensitive to b_d. A 20% error in b_d produces 15 cm s^{-1} uncertainty in the retrieval. In comparison with Table 3, the error resulting from the power-law parameters can be larger than the error resulting from the estimation of W_σ. Assuming the uncertainty from each parameter is independent, the uncertainty from all four parameters and W_σ estimation with 20% error should be 21%, 80%, and ±17 cm s^{-1} for D_{mass}, IWC, and W_m, respectively, using the error propagation law (Bevington and

TABLE 2. The deviations of the retrieval from in situ measurements as well as the mean and standard deviation (right-hand number in the cells) of the five parameters examined (radar moments, temperature T, and normalized distance to cloud top) for the seven classes plotted in Figs. 10 and 11 for both the exponential PSD and gamma PSD function with $\alpha = 5$. The boldface and underline indicate the error and criteria when the gamma PSD with $\alpha = 5$ is applied in the algorithm. See text for additional explanation.

	Exponential PSD retrieval			Indicators to PSD priority					Gamma PSD retrieval ($\alpha = 5$)		
Class	ΔD_{mass} (%)	ΔIWC (%)	ΔW_m (cm s^{-1})	T (K)	Normalized distance to cloud top	Reflectivity (dBZ)	Doppler velocity (cm s^{-1})	Spectrum width (cm s^{-1})	ΔD_{mass} (%)	ΔIWC (%)	ΔW_m (cm s^{-1})
1	−4.1	−3.4	−0.31	228.4/6.1	0.27/0.21	−25.6/7.6	60.8/18.3	27.0/10.1	17.6	20.4	−11.7
2	−14.4	4.5	1.9	229.8/6.5	0.28/0.19	−23.4/7.4	65.2/22.6	29.0/12.1	3.3	36.5	−6.9
3	−26.5	7.3	5.7	232.9/6.0	0.34/0.20	−23.1/9.0	69.4/20.9	27.4/12.1	−8.6	−14.5	−2.0
4	**−37.2**	**8.6**	**9.4**	**235.0/4.4**	**0.39/0.17**	**−20.5/8.4**	**74.1/20.9**	**25.7/10.6**	**−24.4**	**−13.0**	**2.9**
5	−42.2	11.2	13.5	237.0/4.9	0.41/0.15	−17.3/9.2	81.3/23.9	26.1/8.7	−30.7	−9.0	7.9
6	−46.7	24.7	16.8	237.4/3.9	0.45/0.14	−16.8/9.9	77.8/24.9	30.0/16.1	−31.8	−2.6	13.1
7	−54.3	34.4	23.1	237.6/2.5	0.54/0.15	−19.7/9.8	68.9/21.7	33.0/24.7	−38.1	−1.5	20.9

Robinson 1992). These uncertainties are consistent with those predicated from the optical estimation theory (35%, 85%, ±20 cm s^{-1}), assuming 20% variation in the parameters and W_σ, among which a 20% variation in the measurements are assumed.

4. Algorithm validation with in situ measurements

In situ data provide first-hand measurements of cloud particle size and mass. Even though the data may have time or location differences from the ground-based observations and there are often significant uncertainties in the measurements themselves, aircraft data provide the most direct validation of the ground-based retrievals. As an illustration, a case study is presented using MMCR observations on 13 March 2000 at the ARM SGP site. The MMCR reflectivity and the flight track are plotted in Fig. 13. Cirrus clouds in this case are continuous and physically thick. The UND Citation sampled this layer, and only data collected in the horizontal legs are used to validate the algorithm. The in situ air mean velocity and turbulence standard deviation are calculated using Eq. (7) from 15-s averages of 25-Hz Citation data collected during level flight legs. The cloud IWC was measured by the counterflow virtual impactor (CVI; Twohy et al. 1997, 2003); D_{mass} is calculated from the citation PSD and CVI data. The cirrus microphysical properties and the turbulence parameters are retrieved with the current algorithm from MMCR data, which are collocated at the same height and time period with the in situ data. The mean and standard deviation of the empirical parameters used in the retrieval are listed in Table 5. The retrieval is compared with in situ data in histogram plots in Fig. 14. The comparison demonstrates that the algorithm can determine the cloud microphysical properties and air mean velocity with reasonable errors: 50% for IWC, 30% for the particle size, and ±15 cm s^{-1} for the air mean vertical velocity in the radar sampling volume. Even though W_σ is estimated, it is surprisingly in very good agreement with in situ data, which indicates that the error in W_σ introduced by the empirical method described above is small in this case (less than 20%). The retrieved mean error for λ, N_o, and W_m are 50%, 30%, and ±20 cm s^{-1}, respectively. Assuming a 30% error in the parameters of the mass–length relation (a_m, b_m), the derived mass mean length and IWC should have a mean error of 30% and 70%. As a result, the uncertainty from the in situ comparison is within the retrieval error predicted by the optimal estimation framework.

This algorithm is developed for application to tropical cirrus data as well. In situ comparison from one case of aged anvil cirrus is also shown using CRYSTAL FACE data. The CRYSTAL FACE project was designed to study the evolution and radiative properties of the tropical anvil cirrus and took place in south Florida during July 2002. Cirrus on 16 July 2002 were observed by ground-based 94-GHz cloud radar at the western ground site near Everglades City, Florida, from 1840 to 1910 UTC. The retrieved D_{mass}, IWC, and the mean vertical velocity are shown in Fig. 15. The citation spiraled through the cirrus layer (8–12 km) from 1900 to about 2000 UTC, which was about an hour after the clouds were observed by the ground site. The location of the dissipating anvil system was approximately 50 km west of the ground site during the spirals. Even though the location and time of the aircraft and radar observations were not coincident, we found a reasonable agreement between the measured and retrieved IWC and D_{mass}, although the breadth of the in situ data distribution were substantially larger than that found from the ground-based observations (Fig. 16). The turbulence information from the aircraft is not considered to be reliable because the aircraft did not fly level legs through this layer. Another source of uncertainty here

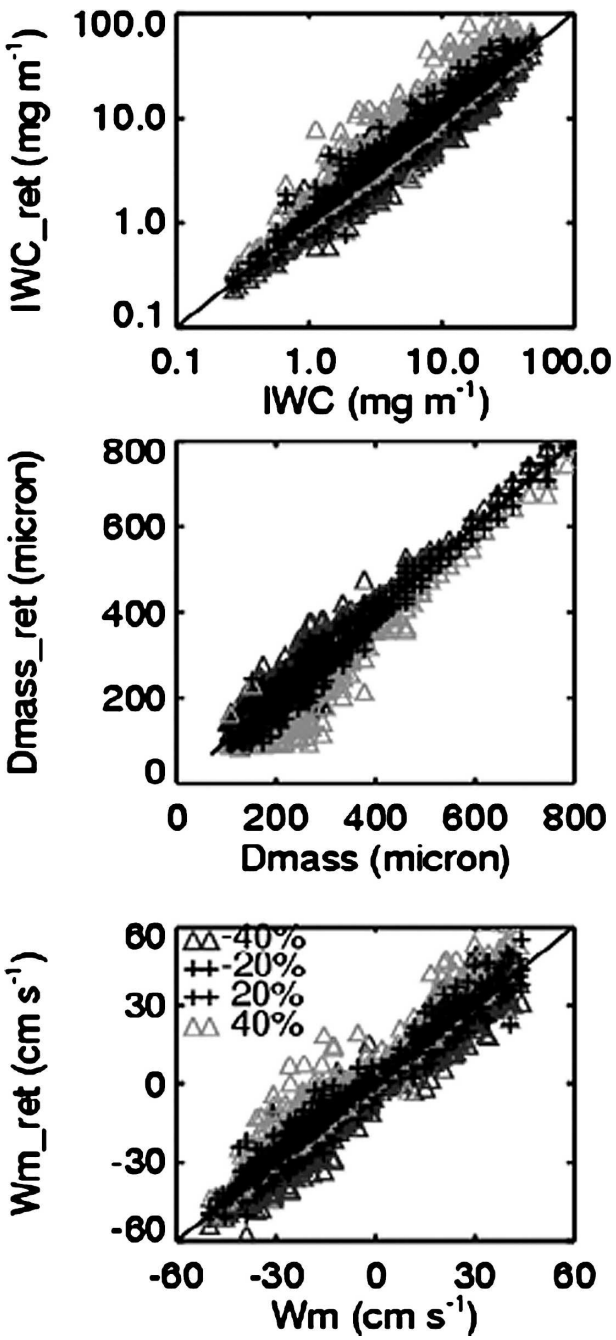

FIG. 12. The algorithm sensitivity to the approximation of W_σ using in situ data on 9 Mar 2000 IOP at ARM SGP. The black solid line is the 1:1 line.

might be resulting from Mie scattering from the 94-GHz cloud radar signal (Kollias et al. 2003), which is not considered in the retrieval algorithm.

5. Summary and conclusions

In this paper, an algorithm using the first three Doppler moments is developed to retrieve cirrus microphysical properties and the mean air vertical motion in the radar sample volume, as well as their errors, simultaneously. As stated in Gossard (1994), the observed Doppler spectrum results from the convolution of a quiet-air radar reflectivity spectrum, determined by the distribution of particle sizes, with the turbulence PDF. However, instead of expressing the convolution integral in terms of the particle fall velocity, we integrate the convolution integral over the air motion so that we can explicitly solve for the mean vertical velocity within the sample volume.

Assuming that the particle size distribution and the turbulence PDF can be approximated with exponential functional shapes, the set of equations describing the Doppler spectrum moments are inverted using optimal estimation theory to derive the particle size distribution, the mean vertical velocity of the air in the sample volume, and objectively derived retrieval error. To avoid an ill condition problem, W_σ is considered as a parameter in the algorithm and is predetermined from the Doppler spectrum width and radar reflectivity based on the observation that the spread of the particle size distribution in the velocity domain dominates the Doppler spectrum width measurement for most cirrus. Based on this approach a method for providing a reasonable first guess for the inversion of the forward model is proposed.

The algorithm is also formulated in terms of a modified gamma distribution of various orders so that the

TABLE 3. The mean and standard deviation (italic) of retrieval from the different W_σ estimations; refer to Fig. 12.

Deviation of W_σ	IWC (mg m^{-3})	W_m (cm s^{-1})	D_{mass} (μm)
−40%	6.91/*7.16*	−14.37/*22.78*	323.75/*182.19*
−20%	7.44/*7.63*	−12.47/*21.94*	312.89/*182.21*
0	8.31/*8.36*	−9.86/*21.78*	298.16/*182.99*
20%	10.07/*10.31*	−6.19/*22.22*	278.13/*184.60*
40%	13.31/*15.18*	−2.02/*23.04*	255.72/*185.48*

TABLE 4. The sensitivity of retrieval to the estimation of the parameters (a_m, b_m, a_d, and b_d). In the parentheses is the fractional error of the parameters. The uncertainty of D_{mass} and IWC is shown in relative deviation (%). For W_m the uncertainty is shown in absolute deviation (cm s^{-1}). The three numbers in each cell are the mean, maximum, and minimum of the deviation from the truth.

Sensitivity	δD_{mass} (%)	δIWC (%)	ΔW_m (cm s^{-1})
a_m (±20%)	0.0/0.0/0.0	26.0/32.0/20.0	0.0/0.0/0.0
b_m (±20%)	17.2/43.6/2.1	75/106/59	11.3/26.0/0.0
a_d (±20%)	1.8/6.7/0.5	2.7/8.8/0.8	1.3/6.0/0.0
b_d (±20%)	7.3/15.5/2.5	11.7/33.8/0.8	15.3/36.0/0.0

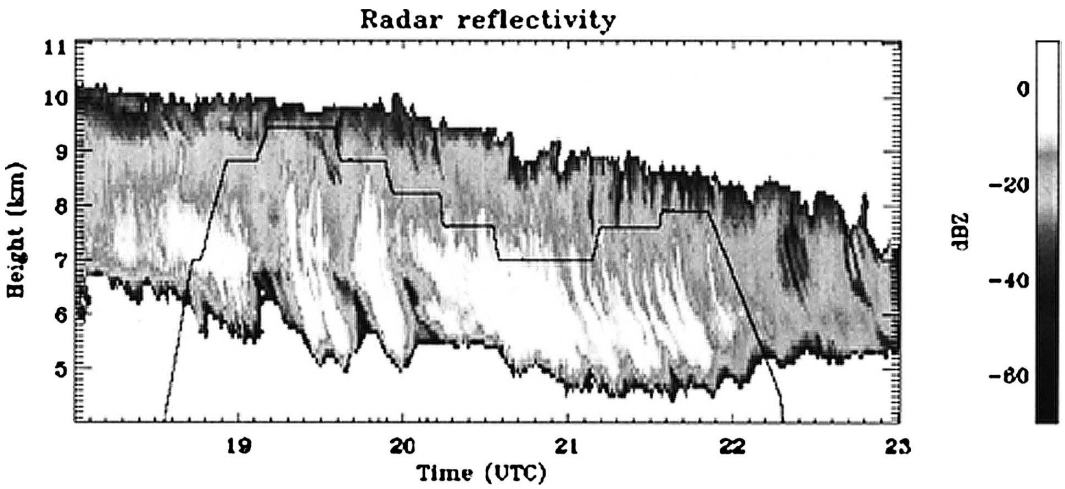

FIG. 13. Radar reflectivity height–time cross section observed by the MMCR on the 13 Mar 2000 IOP at the ARM SGP. The aircraft flight track is overplotted with a black line.

sensitivity to the assumed functional shape of the particle size distribution can be tested using in situ aircraft measurements of cirrus particles and turbulence. We find that single-mode functional shapes as used here more reliably represent the in situ data in the upper two-thirds of cirrus layers, and in such cases an exponential assumption for the particle size distribution produces results as accurate as the modified gamma distribution. In the lower portions of the midlatitude cirrus layers considered, bimodality in the particle size distribution appears to become predominant and neither single-mode functional form represents the measurements very well. It also appears that the IWC can be measured more reliably through a greater depth of the cirrus layer than can the mass mean particle size. A simple set of guidelines for application of the algorithm is presented.

We also test the sensitivity of the algorithm to the parameters in the power-law relationships that describe the ice particle mass and the terminal velocity and W_σ. We show in appendix A that the independent parameters used in this algorithm are those describing the particle mass and cross-sectional area in terms of the particle maximum dimension. We find that the algorithm results are extremely sensitive to the proper choice of these empirical parameters. We emphasize that most retrieval algorithms are very sensitive to these types of assumptions and algorithm error estimates should account for uncertainties in such model assumptions. Given the variability in cirrus microphysical properties, the advent of orbiting active remote sensors (Stephens et al. 2002), and the hyper sensitivity of cloud property retrieval algorithms to such assumptions, there is a pressing need for a more extensive global library of mass- and area-dimensional relationships for use in retrieval algorithms.

TABLE 5. The mean and standard deviation (cgs units) of empirical parameters used in the case of 13 Mar 2000 IOP at the ARM SGP site.

Parameters	Mean	Std dev
a_m	0.0025	0.000 75
b_m	2.114	0.1122
a_d	2.55×10^{-4}	2.8×10^{-5}
b_d	1.23	0.15

Algorithm validation with in situ data is also accomplished using data collected in middle-latitude cirrus and in decaying anvil cirrus. In the middle-latitude case, we are able to examine the validity of the air motion estimates and find a reasonable comparison with in situ data in a particular case. The comparison demonstrates that the algorithm can determine the cloud microphysical properties and air mean velocity with reasonable errors: 50% for IWC, 30% for the particle size, and ± 15 cm s^{-1} for the air mean vertical velocity in the radar sampling volume.

In a following paper, this algorithm is applied to MMCR data collected at ARM sites from the Tropics and middle latitudes. The retrieval dataset is analyzed to examine the difference of cirrus properties at different locations and to develop a potential parameterization of mass-weighted particle fall velocity using temperature and IWC.

Acknowledgments. This research has been supported primarily through the Environmental Science Division of the U.S. Department of Energy (Grant DE-

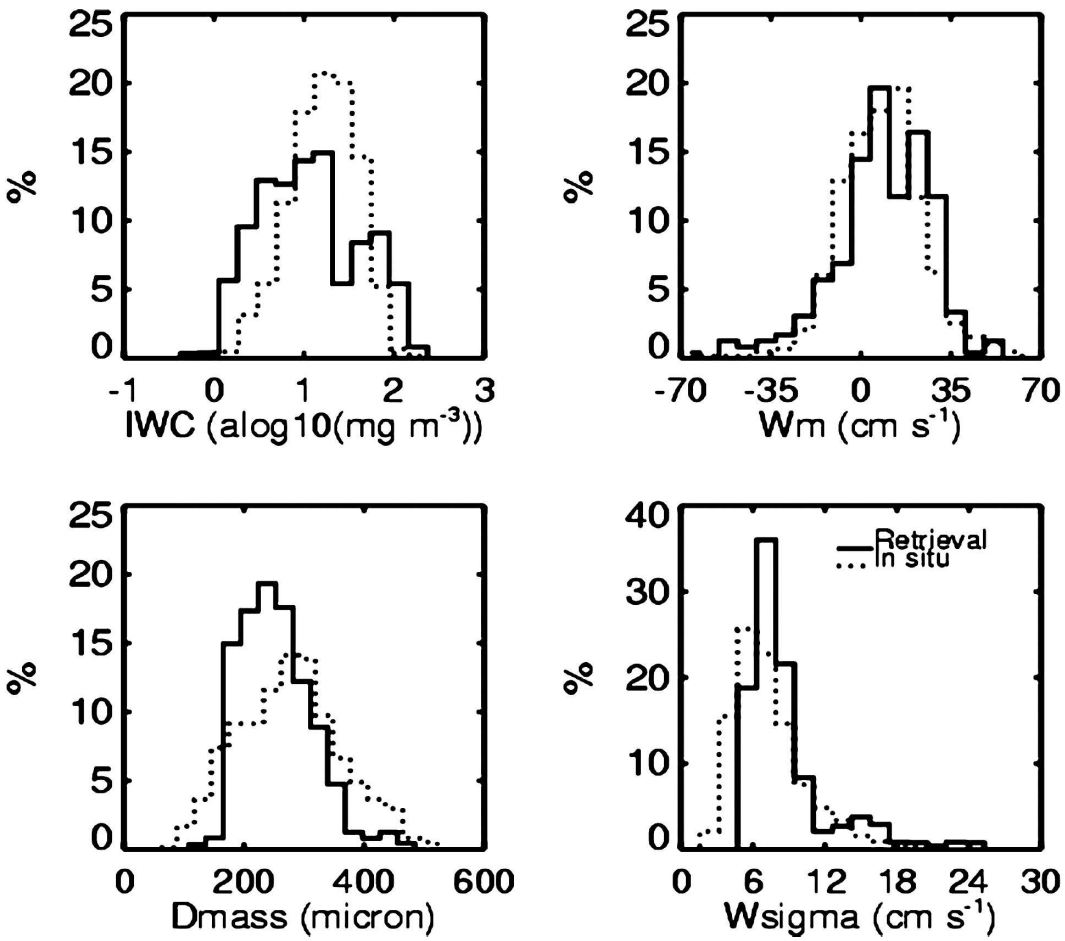

FIG. 14. The histogram comparison between the retrieval and in situ data. The solid line is the retrieval; the dotted line is compiled using data obtained from UND Citation measurements.

FG0398ER62571). This research was also supported by NASA Grants NNG04GG82G and NAG511478. The radar observational data were obtained from the Atmospheric Radiation Measurement Program sponsored by the U.S. Department of Energy, Office of Science, Office of Biological and Environmental Research, Environmental Science Division. The 94-GHz radar observation during CRYSTAL FACE project is provided by R. Marchand from Pacific Northwest National Laboratory. We thank Sally Benson for providing the reconstructed PSD in situ measurements. We thank three reviewers for very constructive suggestions.

APPENDIX A

The Relation between the Power-Law Parameters

As used in Mace et al. (2002) and in this algorithm, there are three sets of parameters from power-law relationships that describe the radar backscattering cross section (a_z, b_z), mass (a_m, b_m), and terminal velocity (a_v, b_v) in terms of the particle maximum dimension D. However, these parameters are not entirely independent of one another. The consistency of these parameters among the relationships is important for the accuracy of the retrieval algorithm results. In this appendix, the relationship between the radar backscattering cross section and the mass-dimensional power-law parameters are derived in two different ways.

a. Through the effective density parameters

The water equivalent radar reflectivity is described as

$$Z_e = \frac{\lambda^4}{\pi^5 |K_w|} \int_0^\infty \sigma_v(D) n(D)\, dD = \int_0^\infty a_z D^{b_z+6} n(D)\, dD, \tag{A1}$$

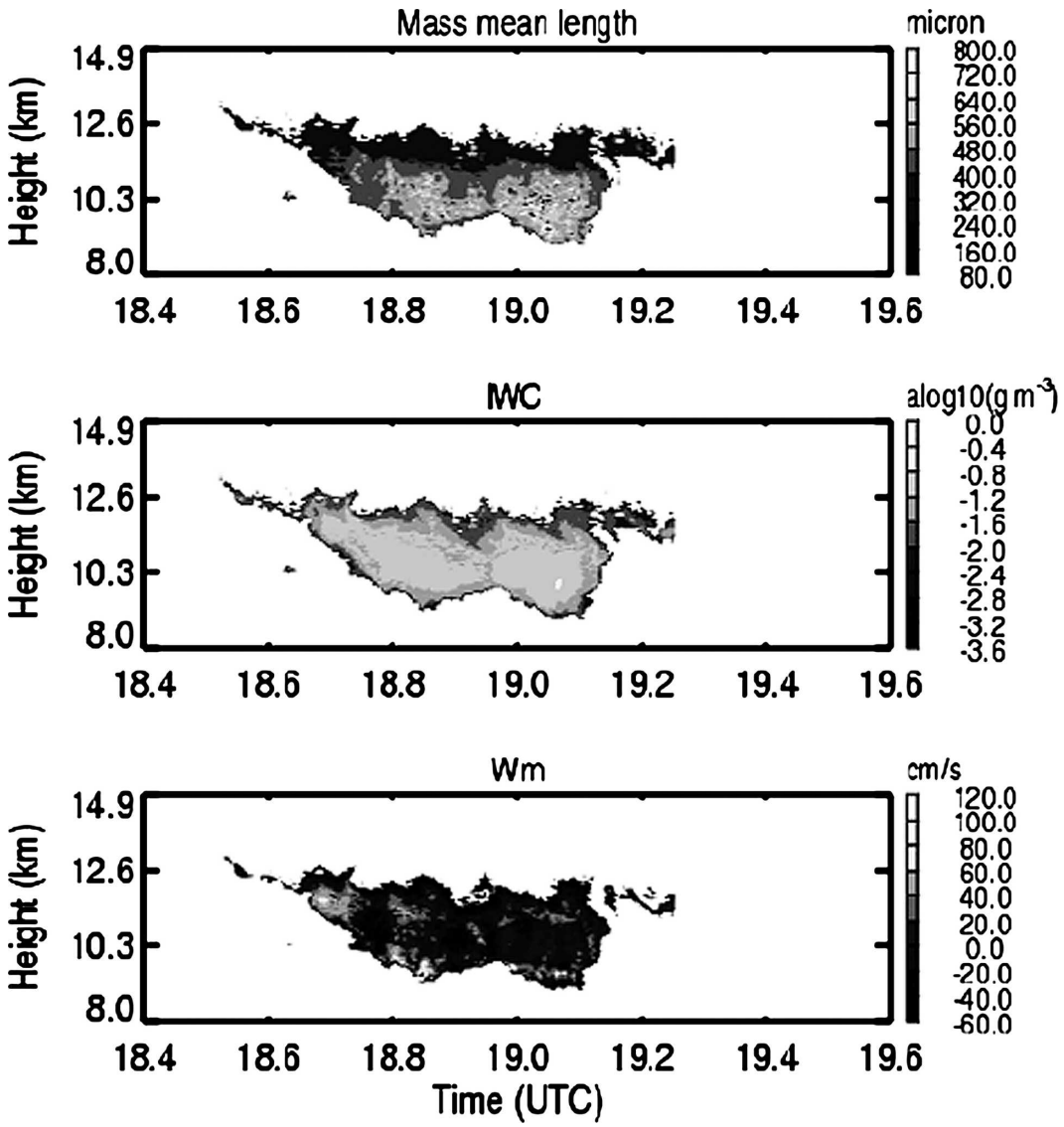

FIG. 15. The retrieved D_{mass}, IWC, and W_m from 95-GHz Doppler radar observation on 16 Jul 2002 during the CRYSTAL FACE project.

where D is the maximum dimension of an ice crystal. The integration in the first part is over the backscattering coefficient σ_v. In Eq. (A1), the radar cross section is parameterized with a power-law fit (Mace et al. 2002), where a_z and b_z are the parameters. For small particles, the radar cross section σ_v can be simplified as

$$\sigma_v = \frac{\pi^5 |K_i|^2}{\lambda^4} D_v^6(D),$$

where D_v is the volume equivalent particle size defined as the diameter of a sphere containing the volume of solid ice composing the nonspherical particle. This assumption is key and is shown to be true for particles less than 800 μm at 35-GHz wavelength (Donovan et al. 2004). Then, Eq. (A1) can be written as

$$Z_e = \int_0^\infty \frac{\lambda^4}{\pi^5 |K_w|^2} |K_i|^2 D_v^6(D) n(D)\, dD$$

$$= \int_0^\infty \frac{|K_i|^2}{|K_w|^2} D_v^6(D) n(D)\, dD. \quad \text{(A2)}$$

The mass-dimensional power-law relationship can convert D_v to maximum dimension D:

$$\rho_{\text{ice}} D_v^3 = \rho_e(D) D^3,$$

where $\rho_e(D)$ is the effective ice particle density (Heymsfield et al. 2004):

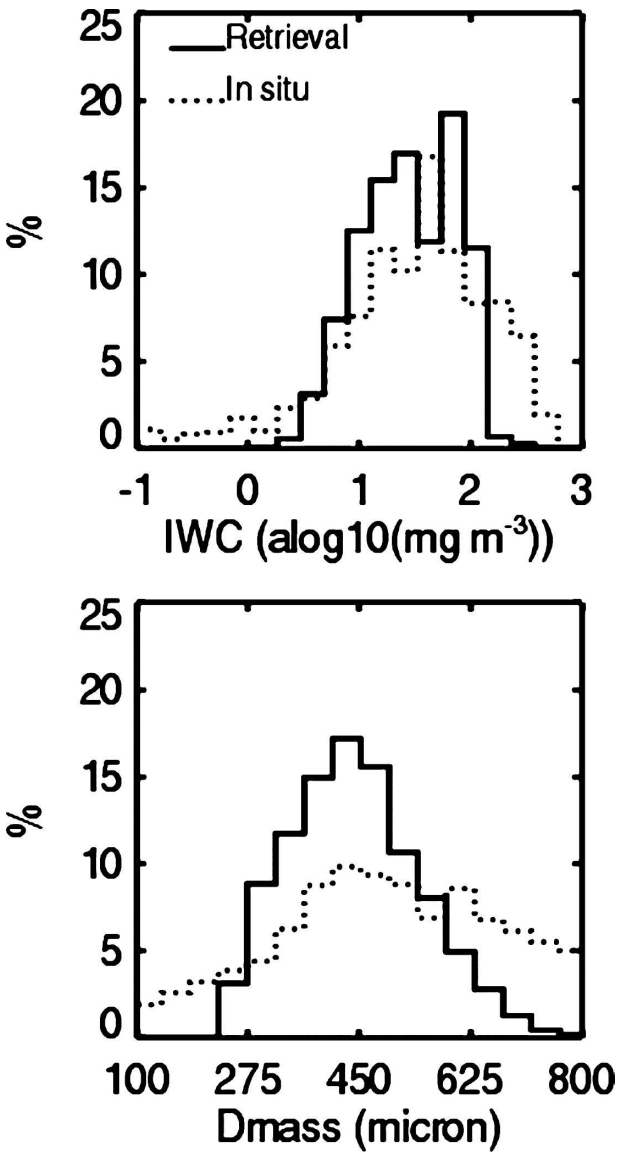

FIG. 16. The retrieved cloud properties comparison with in situ data from 16 Jul 2002 during the CRYSTAL FACE project. The solid-line histogram represents the retrieval results; the dotted-line histogram represents the in situ data.

$$\rho(D) = aD^b,$$

where a and b are the density power-law fit parameters. As a result, Eq. (A2) can be expressed as

$$Z_e = \int_0^\infty \frac{|K_i|^2}{|K_w|^2}\left[\frac{\rho(D)}{\rho_{\text{ice}}}\right]D^6 n(D)\,dD = \int_0^\infty \frac{|K_i|^2}{|K_w|^2}\frac{a^2}{\rho_{\text{ice}}^2}D^{2b+6}n(D)\,dD.$$

In comparing this with Eq. (A1), we get

$$a_z = \frac{|K_i|^2}{|K_w|^2}\frac{a^2}{\rho_{\text{ice}}^2} \quad \text{and} \quad b_z = 2b, \tag{A3}$$

where $K = (m^2 - 1)/(m^2 + 2)$ and m is the complex index of the refraction. At −60°C and 8.5-mm wavelength, the $(K_i/K_w)^2$ is about 0.195.

IWC can be derived using the mass-dimensional power-law relationship:

$$\text{IWC} = \int_0^\infty a_m D^{b_m} n(D)\,dD.$$

With the effective ice particle density, it can also be expressed as

$$\text{IWC} = \int_0^\infty \frac{\pi}{6}D^3\,\rho(D)n(D)\,dD = \int_0^\infty \frac{\pi}{6}aD^{3+6}n\,(D)\,dD.$$

In comparing the above two equations, we have

$$a_m = (\pi/6)a \quad \text{and} \quad b_m = 3 + b. \tag{A4}$$

Using two sets of equations [(A3) and (A4)], we can eliminate a and b and show that

$$a_z = \frac{|K_i|^2}{|K_w|^2}\left(\frac{6}{\pi\rho_{\text{ice}}}\right)^2 a_m^2 \quad \text{and} \quad b_z = 2b_m - 6. \tag{A5}$$

b. Derivation from mass–length relationship

Because of the mass–length relationship

$$V = (\pi/6)D_v^3 = m/\rho_{\text{ice}} = a_m D^{b_m}/\rho_{\text{ice}}, \tag{A6}$$

the radar reflectivity in Eq. (A2) can be written as

$$Ze = \int_0^\infty \frac{|K_i|^2}{|K_w|^2}D_v^6(D)n(D)\,dD = \int_0^\infty \frac{|K_i|^2}{|K_w|^2}\left(\frac{6}{\pi\rho_{\text{ice}}}\right)^2 a_m^2 D^{2b_m}n(D)\,dD.$$

In comparing it with Eq. (A1), we can also obtain

$$a_z = \frac{|K_i|^2}{|K_w|^2}\left(\frac{6}{\pi\rho_{\text{ice}}}\right)^2 a_m^2 \quad \text{and} \quad b_z = 2b_m - 6.$$

The terminal velocity of a particle is determined through a balance between the acceleration of the mass resulting from gravity and the area projected to the airflow that induces drag. Using power-law fits between the Reynolds and Best numbers, Mitchell (1996) demonstrated that the mass- and area-dimensional power laws could be combined to determine ice particle ter-

TABLE B1. List of the variables and constants used in this paper.

Symbol	Unit	Description
		Variables
Z_e	dBZ	The effective radar reflectivity
V_d	cm s^{-1}	Mean Doppler velocity of radar sample volume
σ_d	cm s^{-1}	Doppler spectrum width
N_o	cgs	The particle concentration intercept of exponential PSD
λ	cgs	The slope of exponential PSD
N_g	cgs	Proportionality constant of modified gamma PSD
D_g	cgs	The size where the gamma function maximizes
W_m	cm s^{-1}	The mean air vertical velocity of the radar sample volume
W_σ	cm s^{-1}	The turbulence deviation of the radar sample volume
W_i	cm s^{-1}	Doppler velocity of particles in the radar sample volume
W_j	cm s^{-1}	Air vertical velocity in the radar sample volume
V_f	cm s^{-1}	Particle fall velocity in the radar sample volume
IWC	mg m^{-3}	Ice water content of the radar sample volume
$V_{f\text{mass}}$	cm s^{-1}	Mass-weighted fall velocity of the radar sample volume
D_{mass}	μm	Mass-weighted maximum dimension of the radar sample volume
		Constants
a_m, b_m	cgs	Parameters in the mass–length power-law relationship
a_z, b_z	cgs	Parameters in the backscatter cross-sectional power-law relationship
a_d, b_d	cgs	Parameters in the size and fall velocity power-law relationship
a_v, b_v	cgs	Parameters in the fall velocity and size power-law relationship
a_w, b_w	cgs	Parameters in W_σ estimation as a function in Eq. (20)
α	Unitless	The order in the gamma PSD

minal velocities. Thus, the terminal velocity power-law parameters are not totally independent of the mass-dimensional assumption but do implicitly include information about particle area even though it is not explicitly discussed here.

APPENDIX B

List of the Variables and Constants Used

Table B1 contains a list of the variables and constants used in this paper.

REFERENCES

Ackerman, T. P., K. N. Liou, F. P. J. Valero, and L. Pfister, 1988: Heating rates in tropical anvils. *J. Atmos. Sci.,* **45,** 1606–1623.

Aydin, K., and T. M. Walsh, 1999: Millimeter wave scattering from spatial and planar bullet rosettes. *IEEE Trans. Geosci. Remote Sens.,* **37,** 1138–1150.

Atlas, D., S. Y. Matrosov, A. J. Heymsfield, M.-D. Chou, and D. B. Wolff, 1995: Radar and radiation properties of ice clouds. *J. Appl. Meteor.,* **34,** 2329–2345.

Babb, D. M., and J. Verlinde, 2000: The retrieval of turbulent broadening in radar Doppler using linear inversion with double-sided constraint. *J. Atmos. Oceanic Technol.,* **17,** 1577–1583.

Bevington, P. B., and D. K. Robinson, 1992: *Data Reduction and Error Analysis for the Physical Sciences*. 2d ed. McGraw-Hill, 328 pp.

Boehm, M. T., J. Verlinde, and T. P. Acherman, 1999: On the maintenance of high tropical cirrus. *J. Geophys. Res.,* **104,** 24 423–24 433.

Comstock, J. M., T. P. Ackerman, and G. G. Mace, 2002: Ground based lidar and radar remote sensing of tropical cirrus clouds at Nauru Island: Cloud statistics and radiative impacts. *J. Geophys. Res.,* **107,** 4714, doi:10.1029/2002JD002203.

Del Genio, A. D., M. S. Yao, W. Kovari, and K. K.-W. Lo, 1996: A prognostic cloud water parameterization for global climate models. *J. Climate,* **9,** 270–304.

Donovan, D. P., M. Quante, I. Schimme, and A. Macke, 2004: Use of equivalent spheres to model the relation between radar reflectivity and optical extinction of ice cloud particles. *Appl. Opt.,* **43,** 4929–4940.

Gossard, E. E., 1994: Measurement of cloud droplet size spectra by Doppler radar. *J. Atmos. Oceanic Technol.,* **11,** 712–726.

Gultepe, I., and D. O. Starr, 1995: Dynamical structure and turbulence in cirrus clouds: Aircraft observations during the FIRE. *J. Atmos. Sci.,* **52,** 4159–4182.

Heymsfield, A. J., 1977: Precipitation development in stratiform ice clouds: A microphysical and dynamical study. *J. Atmos. Sci.,* **34,** 367–381.

——, 2003: Properties of tropical and midlatitude ice cloud particle ensembles. Part II: Applications for mesoscale and climate models. *J. Atmos. Sci.,* **60,** 2592–2611.

——, and J. Parrish, 1978: A computational technique for increasing the effective sampling volume of the PMS two-dimensional particel size spectrometer. *J. Geophys. Res.,* **79,** 2199–2206.

——, and L. J. Donner, 1990: A scheme for parameterizing ice-cloud water content in general circulation models. *J. Atmos. Sci.,* **47,** 1865–1877.

——, and J. Iaquinta, 2000: Cirrus crystal terminal velocities. *J. Atmos. Sci.,* **57,** 916–938.

——, C. G. Schmitt, A. Bansemer, D. Baumgardner, E. M. Weinstock, J. T. Smith, and D. Sayres, 2004: Effective ice particle densities for cold anvil cirrus. *Geophys. Res. Lett.,* **31,** L02101, doi:10.1029/2003GL018311.

Jensen, E., O. Starr, and O. B. Toon, 2004: Mission investigates tropical cirrus clouds. *Eos, Trans. Amer. Geophys. Union,* **85,** 45–50.

Kollias, P. B., A. Albrecht, and F. D. Marks Jr., 2003: Cloud radar observations of vertical drafts and microphysics in the convective rain. *J. Geophys. Res.,* **108,** 4053, doi:10.1029/2001JD002033.

Liu, C. L., and A. J. Illingworth, 2000: Toward more accurate retrieval of ice water content from radar measurements of clouds. *J. Appl. Meteor.,* **39,** 1130–1146.

Mace, G. G., T. P. Ackerman, E. E. Clothiaux, and B. A. Albrecht, 1997: A study of composite cirrus morphology using data

from a 94-GHz radar and corrections with temperature and large-scale vertical motion. *J. Geophys. Res.,* **102,** 13 581–13 593.

——, ——, P. Minnis, and D. F. Young, 1998: Cirrus layer microphysical properties derived from surface-based millimeter radar and infrared interferometer data. *J. Geophys. Res.,* **103,** 23 207–23 216.

——, A. J. Heymsfield, and M. R. Poellot, 2002: On retrieving the microphysical properties of cirrus clouds using the moments of the millimeter-wavelength Doppler spectrum. *J. Geophys. Res.,* **107,** 4815, doi:10.1029/2001JD001308.

——, Y. Zhang, S. Plantick, M. D. King, P. Minnis, and P. Yang, 2005: Evaluation of cirrus cloud properties derived from MODIS data using cloud properties derived from ground-based observations collected at the ARM SGP site. *J. Appl. Meteor.,* **44,** 221–240.

——, M. Deng, B. Soden, and E. Zipser, 2006: On the association of tropical cirrus in the 10–15-km layer with deep convective source regions: An observational study combining millimeter radar data and satellite-derived trajectories. *J. Atmos. Sci.,* **63,** 480–503.

Matrosov, S. Y., 1993: Possibilities of cirrus particle sizing from dual-frequency radar measurements. *J. Geophys. Res.,* **98,** 20 675–20 683.

——, 1999: Retrieval of vertical profiles of ice cloud microphysics from radar and IR measurements using tuned regressions between reflectivity and cloud parameters. *J. Geophys. Res.,* **104,** 16 741–16 753.

——, A. V. Korolev, and A. J. Heymsfield, 2002: Profiling cloud ice mass and particle characteristic size from Doppler radar measurements. *J. Atmos. Oceanic Technol.,* **19,** 1003–1018.

Mitchell, D. L., 1996: Use of mass- and area-dimensional power laws for determining precipitation particle terminal velocities. *J. Atmos. Sci.,* **53,** 1710–1723.

Platt, C. M. R., and Harshvardhan, 1988: Temperature dependence of cirrus extinction: Implications for climate feedback. *J. Geophys. Res.,* **98,** 11 051–11 058.

Ramanathan, V., R. D. Cess, E. F. Harrison, P. Minnis, B. R. Barkstrom, E. Ahmad, and D. Hartmann, 1989: Cloud-radiative forcing and climate: Results from the Earth Radiation Budget Experiment. *Science,* **243,** 57–63.

Randall, D. A, Harshvardhan, D. A. Dazlich, and T. G. Corsetti, 1989: Interactions among radiation, convection and large-scale dynamics in a general circulation model. *J. Atmos. Sci.,* **46,** 1943–1970.

Rodgers, C. D., 2000: *Inverse Methods for Atmospheric Sounding: Theory and Practice*. Series on Atmospheric Oceanic and Planetary Physics, Vol. 2, World Scientific, 238 pp.

Stephens, G. L., and Coauthors, 2002: The CloudSat mission and the A-train: A new dimension of space-based observations of clouds and precipitation. *Bull. Amer. Meteor. Soc.,* **87,** 1771–1790.

Stokes, G. M., and S. E. Schwartz, 1994: The Atmospheric Radiation Measurement (ARM) Program: Programmatic background and design of the cloud and radiation test bed. *Bull. Amer. Meteor. Soc.,* **75,** 1201–1221.

Twohy, C. H., A. J. Schanot, and W. A. Copper, 1997: Measurement of condensed water content in liquid and ice clouds using an airborne counterflow virtual impactor. *J. Atmos. Oceanic Technol.,* **14,** 197–202.

——, J. W. Strapp, and M. Wendisch, 2003: Performance of a counterflow virtual impactor in the NASA icing research tunnel. *J. Atmos. Oceanic Technol.,* **20,** 781–790.

Wang, Z., and K. Sassen, 2002: Cirrus cloud microphysical property retrieval using lidar and radar observation. Part I: Algorithm description and comparison with in situ data. *J. Appl. Meteor.,* **41,** 218–229.

——, D. N. Whiteman, B. B. Demoz, and I. Veselovskii, 2004: A new way to measure cirrus cloud ice water content by using ice Raman scatter with Raman lidar. *Geophys. Res. Lett.,* **31,** L15101, doi:10.1029/2004GL020004.

Warren, S. G., C. J. Hahn, and J. London, 1985: Simultaneous occurrence of different cloud types. *J. Climate Appl. Meteor.,* **24,** 658–667.

Zhang, Y., and G. G. Mace, 2006: Retrieval of cirrus microphysical properties with a suite of algorithms for airborne and spaceborne lidar, radar, and radiometer data. *J. Appl. Meteor. Climatol.,* **45,** 1665–1689.